Atmos. Chem. Phys., 16, 8461–8478, 2016
www.atmos-chem-phys.net/16/8461/2016/
doi:10.5194/acp-16-8461-2016

Atmospheric Chemistry and Physics
Open Access
EGU

Investigation of processes controlling summertime gaseous elemental mercury oxidation at midlatitudinal marine, coastal, and inland sites

Zhuyun Ye[1], Huiting Mao[1], Che-Jen Lin[2,3], and Su Youn Kim[4]

[1]Department of Chemistry, State University of New York, College of Environmental Science and Forestry, Syracuse, NY 13210, USA
[2]Center for Advances in Water and Air Quality, Lamar University, Beaumont, TX 77710, USA
[3]Department of Civil and Environmental Engineering, Lamar University, Beaumont, TX 77710, USA
[4]R&D Program Evaluation Division Office of National Evaluation and Analysis Korea Institute of S&T Evaluation and Planning (KISTEP), Seoul, South Korea

Correspondence to: Huiting Mao (hmao@esf.edu)

Received: 13 October 2015 – Published in Atmos. Chem. Phys. Discuss.: 15 January 2016
Revised: 31 May 2016 – Accepted: 17 June 2016 – Published: 12 July 2016

Abstract. A box model incorporating a state-of-the-art chemical mechanism for atmospheric mercury (Hg) cycling was developed to investigate the oxidation of gaseous elemental mercury (GEM) at three locations in the northeastern United States: Appledore Island (AI; marine), Thompson Farm (TF; coastal, rural), and Pack Monadnock (PM; inland, rural, elevated). The chemical mechanism in this box model included the most up-to-date Hg and halogen chemistry. As a result, the box model was able to simulate reasonably the observed diurnal cycles of gaseous oxidized mercury (GOM) and chemical speciation bearing distinct differences between the three sites. In agreement with observations, simulated GOM diurnal cycles at AI and TF showed significant daytime peaks in the afternoon and nighttime minimums compared to flat GOM diurnal cycles at PM. Moreover, significant differences in the magnitude of GOM diurnal amplitude (AI > TF > PM) were captured in modeled results. At the coastal and inland sites, GEM oxidation was predominated by O_3 and OH, contributing 80–99 % of total GOM production during daytime. H_2O_2-initiated GEM oxidation was significant (∼ 33 % of the total GOM) at the inland site during nighttime. In the marine boundary layer (MBL) atmosphere, Br and BrO became dominant GEM oxidants, with mixing ratios reaching 0.1 and 1 pptv, respectively, and contributing ∼ 70 % of the total GOM production during midday, while O_3 dominated GEM oxidation (50–90 % of GOM production) over the remaining day when Br and BrO mixing ratios were diminished. The majority of HgBr produced from GEM+Br was oxidized by NO_2 and HO_2 to form brominated GOM species. Relative humidity and products of the CH_3O_2+BrO reaction possibly significantly affected the mixing ratios of Br or BrO radicals and subsequently GOM formation. Gas–particle partitioning could potentially be important in the production of GOM as well as Br and BrO at the marine site.

1 Introduction

Mercury (Hg) is a toxic pollutant found globally in air, natural waters, and soils. The health concern regarding Hg arises from the neurotoxic organic form, methyl mercury (MeHg), in the aquatic environments (Mason et al., 2006; Miller et al., 2007; Rolfhus et al., 2003). The high bioaccumulation and biomagnification of MeHg leads to human exposure through the consumption of seafood (Clarkson, 1994). Deposition of atmospheric Hg is one of the most important sources of aquatic Hg.

In the atmosphere, Hg exists in three forms: gaseous elemental mercury (GEM), gaseous oxidized mercury (GOM), and particulate bound mercury (PBM). The majority of atmospheric Hg is GEM, comprising > 95 % of total gaseous mercury (TGM = GEM + GOM). The 0.8–1.7 years atmospheric lifetime of GEM is conducive to long-range transport of Hg as a global pollutant (Bergan et al., 1999; Bergan and Rodhe, 2001; Holmes et al., 2006; Lin and Pehkonen,

1999; Schroeder and Munthe, 1998; Selin et al., 2007). In contrast, GOM and PBM are relatively short-lived and subject to wet deposition and stronger dry deposition than GEM due to their high solubility in water and low vapor pressure. GOM in the atmosphere can be produced from oxidation of GEM, released directly from anthropogenic emissions, and transformed from PBM. In remote regions, in situ GOM production may be the major source of GOM (Weiss-Penzias et al., 2003; Poissant et al., 2005; Mao and Talbot, 2012) considering its short lifetime.

Chemical speciation of atmospheric Hg is essential to understanding its geochemical cycle. Theoretical and experimental studies suggested that the main oxidants of GEM in the atmosphere are ozone (O_3), hydroxyl radical (OH), atomic bromine (Br), bromine monoxide (BrO), hydrogen peroxide (H_2O_2), and atomic chlorine (Cl), yielding GOM species of HgO, HgBrO, HgBr, $Hg(OH)_2$, and HgCl as well as through further reaction with other mercury halides (Ariya et al., 2015; Dibble et al., 2012; Lin and Pehkonen, 1999). Although efforts have been made to investigate the relative importance of these oxidants for GEM oxidation in the troposphere, it is still not well understood. In the terrestrial environment, it was suggested that the oxidation of GEM was primarily by O_3 and OH radicals (Shon et al., 2005; Sillman et al., 2007). The speciation and quantification of GEM + O_3 product(s) still remain unknown and debatable (Ariya et al., 2015; Gustin et al., 2013; Rutter et al., 2012). An experimental study by Pal and Ariya (2004b) measured 1 % of HgO produced by GEM + O_3 on an aerosol filter. Snider et al. (2008) showed the production of HgO(s) in their kinetic and product study. Schroeder et al. (1998) suggested HgO would not exist as an isolated molecule in the gas phase but could be deposited to and retained by the manifold given a decomposition temperature of +500 °C. However, the GEM + O_3 reaction and decomposition temperature (Schroeder et al., 1998) could also be impacted by the presence of other ambient gases (Snider et al., 2008; Gustin et al., 2013; Seigneur et al., 1994). A recent study of Huang et al. (2013) using nylon and cation exchange membranes observed gas-phase HgO. The reaction of GEM + OH has been the subject of debate between theoretical and experimental studies, as no mechanism consistent with thermochemistry has been proposed (Ariya et al., 2015; Pal and Ariya, 2004a; Subir et al., 2011). Measurement studies on GOM in polar regions (Simpson et al., 2007; Steffen et al., 2008) and the subtropical marine boundary layer (MBL; Laurier et al., 2003; Laurier and Mason, 2007; Obrist et al., 2011) as well as atmospheric modeling studies on mercury cycling (Holmes et al., 2009, 2010; Kim et al., 2010; Lindberg et al., 2002; Obrist et al., 2011; Soerensen et al., 2010; Toyota et al., 2014; Wang et al., 2014; Xie et al., 2008) have suggested Br as an important oxidant of GEM. The major source of atmospheric Br was suggested to be produced photolytically from Br-containing compounds and through the Br–BrO cycle involving tropospheric O_3 (Saiz-Lopez and von Glasow, 2012; Simpson et al., 2015).

GOM concentrations and speciation could be impacted by meteorological conditions and chemical conditions in different environments. High solubility of GOM species and possible phase partitioning of HgO as discussed above could both be the reasons causing varying GOM speciation at different locations. For instance, the aerosol type, size distribution, and chemical composition varied largely between the MBL site and inland sites, which may lead to different gas–particle partitioning rates of GOM species.

Hg chemistry in the MBL, the lowest part of the troposphere in direct contact with the sea surface, has global importance as approximately 70 % of the earth's surface is covered by oceans (Glasow et al., 2002). Hg in the MBL cycles differently from in coastal or inland areas. However, contemporary models are not able to reproduce GOM observations temporally and spatially due to knowledge gaps in Hg science, simplified model assumptions, and uncertainties of measurements (Ariya et al., 2015; Lin et al., 2006). In the polar region, bromine radicals were identified as the primary cause of the Arctic mercury depletion events (AMDE) (Kim et al., 2010; Lindberg et al., 2002; Toyota et al., 2014; Xie et al., 2008). In the MBL outside polar regions, due to lower mixing ratios of atmospheric halogen radicals, often lower than the detection limit, mechanisms for GOM production were more controversial than in polar regions. Using a box model, Hedgecock et al. (2003) and Hedgecock and Pirrone (2004, 2005) suggested that O_3 was a dominant GEM oxidant in the MBL at midlatitudes in the Mediterranean region and that the GEM + O_3 reaction may form solid products. However, the reaction kinetics in their model were out of date, with limited halogen chemistry, and the fixed emissions used in the model oversimplified the source terms. Holmes et al. (2009) simulated that GEM oxidation by Br comprised 35–60 % of the GOM sources using BrO concentrations calculated at a photostationary state from a prescribed distribution of Br mixing ratios. Additionally, a parameter was introduced in the same study to account for the entrainment of free-tropospheric GOM into the MBL, and the Br mixing ratio was adjusted to capture the observed GOM diurnal trend, which could cause large uncertainties in GOM simulations. Most recently, Wang et al. (2014) employed updated Hg reactions together with bromine and iodine reactions, adopting the free-tropospheric GOM entrainment parameter from Holmes et al. (2009) for tropical MBL, and found Br to be a primary GEM oxidant, but oxidation by Br or O_3/OH alone was unable to reproduce observed GOM concentration. However, different GEM oxidants could be dominant in different environments, as a result of the unique composition and concentration levels of in situ oxidants those environments may be characterized with.

In this study, we employed a state-of-the-art chemical mechanism that incorporates gas- and aqueous-phase chemistry of Hg, O_3, and halogen to investigate the dynamics

of GOM formation under various atmospheric conditions in midlatitude regions. The most up-to-date kinetics was applied. Halogen radical mixing ratios (such as Br and BrO) were calculated using up-to-date atmospheric halogen reactions. Clear-sky days with calm wind conditions were selected, which are mostly associated with strong atmospheric stability, to minimize the entrainment effect of free-tropospheric air and regional transport, and hence no entrainment factor was included in this study. Moreover, the initial GEM mixing ratios along with a list of compounds (Table 2) in the model were obtained from observations in three different environments and were set to be constant during simulations. Fixing the input concentrations of GEM among a number of other compounds (Table 2) as constants using observational data enabled a modeled chemical environment close to the real atmospheric environment that is being studied. Moreover, a box model simulates the concentrations of short-lived compounds reaching an instantaneous chemical steady state, and for the timescales of such instants, the chemicals such as GEM are long-lived enough to maintain a constant level. In Sect. 2, the methods employed were laid out in detail. Section 3 presented results of reasonably simulated differences between GOM diurnal cycles at the three locations that were captured in measurement data, major GEM oxidants in the three environments, and a detailed discussion of the sensitivity of physical parameters and important chemical reactions. Section 4 summarized the key findings and implications from this study.

2 Methods

2.1 Box model description

The Kinetic PreProcessor version 2.1 (Sandu and Sander, 2006) was utilized as the framework of the box model (Hedgecock et al., 2003; Hedgecock and Pirrone, 2004, 2005). A second-order Rosenbrock method (Verwer et al., 1999) was applied to solve the coupled ordinary differential equations. The box model used in this study was initially set up by Kim et al. (2010). It was further improved in this study by incorporating the most up-to-date gas- and aqueous-phase chemical mechanisms (Atkinson et al., 2004, 2008; Dibble et al., 2012; Sander et al., 2011) to the model.

2.1.1 Reactions and kinetics

The box model has a total of 424 reactions: 276 gas-phase reactions (including Hg, halogen, O_3, sulfate, and hydrocarbon reactions), 52 gas–water equilibriums, 28 aqueous equilibriums, and 68 aqueous reactions. Most of these reactions and kinetic data were updated based on JPL Report No. 17 (Sander et al., 2011), the halogen chemistry reviews of Atkinson et al. (2004, 2008), and the references listed in Table 1. Photodissociation coefficients were calculated from the Tropospheric Ultraviolet and Visible (TUV) Radiation Model (Madronich, 1993).

The most important improvements in chemistry are the gas and aerosol phase of Hg and halogen reactions. Gas-phase Hg reactions included in the box model are (Table 1) as follows:

1. oxidation of GEM by O_3, OH, H_2O_2, Br, BrO, Cl, Cl_2, and I (G1–8);
2. reduction of HgBr and HgI to produce GEM (G9–11); and
3. reactions of HgBr/HgCl with BrO, ClO, IO, NO_2, HO_2, and OH (G12–24) with kinetics suggested by Dibble et al. (2012).

Aqueous Hg reactions include (Table S1 in the Supplement)

1. oxidations of Hg by O_3, OH, HOCl, and ClO^- as well as further oxidation of HgOH by O_2;
2. reduction of Hg^{2+} by HO_2 and photolytic reduction of $Hg(OH)_2$ and S(IV)-mediated reduction; and
3. aqueous equilibria involving $HgSO_3$, $Hg(SO_3)_2^{2-}$, $HgOH^+$, and $Hg(OH)_2$. Gas-phase halogen reactions in the box model are mainly cycles of halogen radicals (Cl/Br/I and ClO/BrO/IO radicals).

The Cl/Br/I radical cycles include photodissociation of Cl_2/Br_2/I_2, organic halides, and other inorganic halides as sources and oxidation reactions as sinks. The ClO/BrO/IO radical cycles involve the oxidation of Cl/Br/I radicals, photodissociation of $ClNO_2$/$ClONO_2$/$BrNO_2$/$BrONO_2$, production from other halogen radicals, and sink reactions to calculate Cl/Br/I radicals or other halides. Aqueous halogen reactions include reactions of Br^-/Cl^- and reactions of aqueous BrCl, HCl, HBr, HOCl, HOBr, Cl_2, and Br_2 species. The chemistry of halogen radicals, especially the reaction cycles of Br and BrO radicals, could be important and should not be neglected or replaced by simple approximation. Hence, the most up-to-date halogen chemistry from the literature was included in our model.

2.1.2 Initial conditions and input data

Observations at three sites from the University of New Hampshire (UNH) AIRMAP Observing Network (http://www.eos.unh.edu/observatories/data.shtml) were used: a marine site located on Appledore Island (AI) at the Shoals Marine Lab, the Gulf of Maine (42.97° N, 70.62° W; 40 m a.s.l.); a coastal site located in Thompson Farm (TF) in Durham, NH (43.11° N, 70.95° W; 24 m a.s.l.) and 25 km away from the Gulf of Maine; and a forested site 90 km inland located on Pack Monadnock (PM) in Miller State Park in Peterborough, NH (42.86° N, 71.88° W; 700 m a.s.l.)

Table 1. Gas-phase Hg reactions in the box model.

No.	Reactions	Kinetic (cm^3 $molecule^{-1}$ s^{-1})	Reference
G1	$Hg + O_3 \rightarrow HgO + O_2$	$8.43 \times 10^{-17} e^{-1407/T}$	Snider et al. (2008)
G2	$Hg + OH\ \{ + O_2 \} \rightarrow HgO + HO_2$	$3.55 \times 10^{-14} e^{294/T}$	Pal and Ariya (2004a)
G3	$Hg + H_2O_2 \rightarrow Hg(OH)_2$	8.5×10^{-19}	Tokos et al. (1998)
G4	$Hg + Cl \rightarrow HgCl$	$6.4 \times 10^{-13} e^{(680 \times (1/T - 1/298))}$	Donohoue et al. (2005)
G5	$Hg + Cl_2 \rightarrow HgCl_2$	2.6×10^{-18}	Ariya et al. (2002)
G6	$Hg + Br \rightarrow HgBr$	$3.7 \times 10^{-13} (T/298)^{-2.76}$	Goodsite et al. (2004, 2012)
G7	$Hg + BrO \rightarrow HgBrO$	1.8×10^{-14}	Raofie and Ariya (2004)
G8	$Hg + I \rightarrow HgI$	$4.0 \times 10^{-13} (T/298)^{-2.38}$	Goodsite et al. (2004)
G9	$HgI \rightarrow Hg + I$	$3.0 \times 10^{9} e^{-3742/T}$	Goodsite et al. (2004)
G10	$HgBr \rightarrow Hg + Br$	$1.6 \times 10^{-9} e^{-7801/T} \times [M]$	Dibble et al. (2012)
G11	$HgBr + Br \rightarrow Hg + Br_2$	3.89×10^{-11}	Balabanov et al. (2005)
G12	$HgBr + Br \rightarrow HgBr + Br$	3.97×10^{-11}	Balabanov et al. (2005)
G13	$HgBr + Br \rightarrow HgBr_2$	2.98×10^{-11}	Balabanov et al. (2005)
G14	$ClO + HgCl \rightarrow ClHgOCl$	5.0×10^{-11}	Dibble et al. (2012)
G15	$ClO + HgBr \rightarrow BrHgOCl$	5.0×10^{-11}	Dibble et al. (2012)
G16	$BrO + HgCl \rightarrow BrHgOCl$	1.09×10^{-10}	Dibble et al. (2012)*
G17	$BrO + HgBr \rightarrow BrHgOBr$	1.09×10^{-10}	Dibble et al. (2012), Wang et al. (2014)
G18	$NO_2 + HgCl \rightarrow ClHgNO_2$	8.6×10^{-11}	Dibble et al. (2012)*
G19	$NO_2 + HgBr \rightarrow BrHgNO_2$	8.6×10^{-11}	Dibble et al. (2012), Wang et al. (2014)
G20	$HO_2 + HgCl \rightarrow ClHgOOH$	8.2×10^{-11}	Dibble et al. (2012)*
G21	$HO_2 + HgBr \rightarrow BrHgOOH$	8.2×10^{-11}	Dibble et al. (2012), Wang et al. (2014)
G22	$OH + HgCl \rightarrow ClHgOH$	6.33×10^{-11}	Dibble et al. (2012)*
G23	$OH + HgBr \rightarrow BrHgOH$	6.33×10^{-11}	Dibble et al. (2012), Wang et al. (2014)
G24	$IO + HgBr \rightarrow BrHgOI$	4.9×10^{-11}	Wang et al., 2014

* The kinetic data of these HgCl reactions were not included in Dibble et al. (2012); they were assumed to be the same kinetic as the HgBr reactions, which were calculated by Wang et al. (2014).

(Fig. 1). Hourly mean values of GEM, O_3, CO, NO, and meteorological observations (i.e., temperature, relative humidity, and solar radiation) at these three sites were used as initial input to the box model. For species that were not measured, we set their initial concentrations as the values in similar environments from the literature if available. Observations of GOM mixing ratios from the three sites were utilized to evaluate the model performance. GEM and GOM data were collected using the Tekran® 2537/1130/1135 speciation unit (Tekran Inc., Canada). For these three sites, the instruments were first run and calibrated in the laboratory and then operated at the sites in a consistent manner. GEM was measured at 5 min intervals and with a limit of detection (LOD) of ∼ 5–10 ppqv (Mao et al., 2008); GOM was measured over a 2 h sampling period with an LOD of ∼ 0.1 ppqv based on 3 times the standard deviation of the field blank values (Sigler et al., 2009; Mao and Talbot, 2012). A custom-built refrigerator assembly and a canister of drierite was used to cool and dry air streams before they entered into the 1130 pump module, resulting in < 25 % RH of air streams (Sigler et al., 2009). Detailed information on these measurements can be found in Mao and Talbot (2004, 2012), Talbot et al. (2005), Fischer et al. (2007), Mao et al. (2008), and Sigler et al. (2009). Table 2 lists the input variables of the box model. The model's initial mixing ratios of GEM, O_3, CO, and NO were obtained from observations and were set to be constant during each 1 h simulation. Br/Cl/I concentrations were all calculated from the model given initial concentrations of 1 pptv (Finley and Saltzman, 2008; except for AI) for Br_2, Cl_2, and I_2 species. At AI, the Br_2 initial concentration was set to be constant during simulations and used the values of Saiz-Lopez et al. (2006) to constrain [BrO]. Detailed information can be found in Sect. 3.3.1. Dry-deposition flux was calculated using dry-deposition velocity data derived from Zhang et al. (2009, 2012) and boundary layer height estimated from Mao and Talbot (2004). Other physical parameters (i.e., Henry's constants, liquid water content, and aerosol radius) were used to simulate the gas–particle partitioning process in the box model.

2.1.3 Gas–particle partitioning

An empirical expression was utilized to calculate particle size growth relative to its dry radius (r_{dry}) (Lewis and Schwartz, 2006):

$$r = r_{dry} \frac{4}{3.7} \left(\frac{2 - RH}{1 - RH} \right)^{\frac{1}{3}}, \quad (1)$$

Table 2. Box model input and simulated variables.

Parameter	Appledore Island (AI)	Thompson Farm (TF)	Pack Monadnock (PM)
Observed[a]			
RH, relative humidity	76.9 ± 5.4	69.9 ± 19.5	69.0 ± 13.1
Temperature, °C	19.1 ± 1.7	21.3 ± 4.3	18.5 ± 3.3
[GEM], ppqv	133.9 ± 3.3	138.4 ± 12.8	149.6 ± 3.2
[O_3], ppbv	37.4 ± 8.8	32.7 ± 15.7	45.0 ± 4.2
[NO], pptv	154.5[b]	232.4 ± 364.1	85.3 ± 35.8
[CO], ppbv	169.6 ± 13.9	156.2 ± 10.8	120.2 ± 7.2
Simulated[c]			
[Br], ppqv	28.50	0.20	0.18
[OH], ppqv	100.7	75.8	73.5
Other[d]			
v_d, $cm\,s^{-1}$, dry-deposition velocity	GEM – 0.0045	GEM – 0.07	GEM – 0.08
	GOM – 0.5	GOM – 1.2	GOM – 2.0
	PBM – 0.5	PBM – 0.15	PBM – 0.25
H, $M\,atm^{-1}$, Henry's constants	HgO -3.2×10^9	HgO -3.2×10^9	HgO -3.2×10^9
	$Hg(OH)_2 - 1.2 \times 10^7$	$Hg(OH)_2 - 1.2 \times 10^7$	$Hg(OH)_2 - 1.2 \times 10^7$
	Other GOM -2.7×10^9	Other GOM -2.7×10^9	Other GOM -2.7×10^9
L, $m^3_{water} m^{-3}_{air}$, liquid water content	5×10^{-11}	2.0×10^{-11}	1.25×10^{-11}
D_g, $m^2\,s^{-1}$, diffusion coefficient	1×10^{-5}	1×10^{-5}	1×10^{-5}
Z, m, boundary layer height	500	200–1120[e]	100
r_{dry}, μm, dry aerosol radius	3.5	0.3	0.07

[a] Observed 24 h mean values for all studied cases at these sites. [b] Missing NO measurements at AI; 154.5 ppqv are used for initial values. [c] Simulated 24 h mean values for all studied days at these sites. [d] Reference: Baumgardner et al. (2000), Kim et al. (2012), Mao and Talbot (2004), Moldanová and Ljungström (2001), Pillai and Moorthy (2001), Shon et al. (2005), Zhang et al. (2009, 2012). [e] TF boundary layer height changed at each hour, the averaged diurnal cycle was obtained from Research Data Archive at the National Center for Atmospheric Research, http://rda.ucar.edu/.

where RH is the relative humidity and r is the particle radius at RH.

Gas–particle partitioning was treated by mass transfer between droplets and air. The dynamic mass transfer coefficient across the gas–aqueous interface was calculated using the method developed by Schwartz (1986). The net mass flux (F, molecule $cm^{-3}\,s^{-1}$) between the gas and aqueous phase is given by

$$F = k_{mt} \times \left(L \times c_g - \frac{c_{aq}}{HRT}\right), \quad (2)$$

where L is the liquid water content ($m^3_{water} m^{-3}_{air}$), k_{mt} is the mass transfer coefficient (s^{-1}), c_g is the gas-phase concentration of the species (molecules cm^{-3}), c_{aq} is the aqueous-phase concentration of species (molecules cm^{-3}), H is the Henry's constant of the species ($M\,atm^{-1}$), R is the universal gas constant ($atm\,L\,K^{-1}\,mol^{-1}$), and T is atmospheric temperature (K). k_{mt} is calculated as follows:

$$k_{mt} = \left(\frac{r^2}{3D_g} + \frac{4r}{3\overline{v}\alpha}\right)^{-1}, \quad (3)$$

$$\overline{v} = \left(\frac{8RT}{M\pi}\right)^{\frac{1}{2}}, \quad (4)$$

where r is the particle radius (μm), D_g is the diffusion coefficient ($m^2\,s^{-1}$), $\overline{v}$ is the mean thermal molecular velocity ($m\,s^{-1}$), α is the dimensionless accommodation coefficient, and M is the species molecular weight ($g\,mol^{-1}$).

2.2 Case selection

A total of 83 cases were examined to investigate the role of chemistry in Hg cycling in the MBL and in coastal and inland environments. At the study sites, significant warm season declines in GEM were observed with annual maximums in spring and minimums in autumn, resulting in seasonal amplitudes up to 100 ppqv at TF (Mao et al., 2008). The lost GEM during the warm season most likely entered the ecosystem. Chemical transformation of GEM in warm seasons was suspected to be one of the factors causing the observed seasonal decline in GEM. As such, this study selected the cases representing summer days when chemical processes were most likely dominant. To exclude the influence of wet deposition, we selected clear-sky conditions based on the observed photodissociation rate constant of NO_2 (jNO_2) and solar radiation flux. To minimize the influence of transport, cases with arithmetic daily mean wind speed higher than the 75th percentile of all summer days in studied years ($>1.3\,m\,s^{-1}$ at TF, $>6\,m\,s^{-1}$ at PM, and $>7\,m\,s^{-1}$ at AI) were excluded. As a result, 50, 12, and 21 clear-sky days at AI (marine), TF (coastal), and PM (inland, elevated), respectively, were selected from the summers of 2007, 2008, and 2010. Since

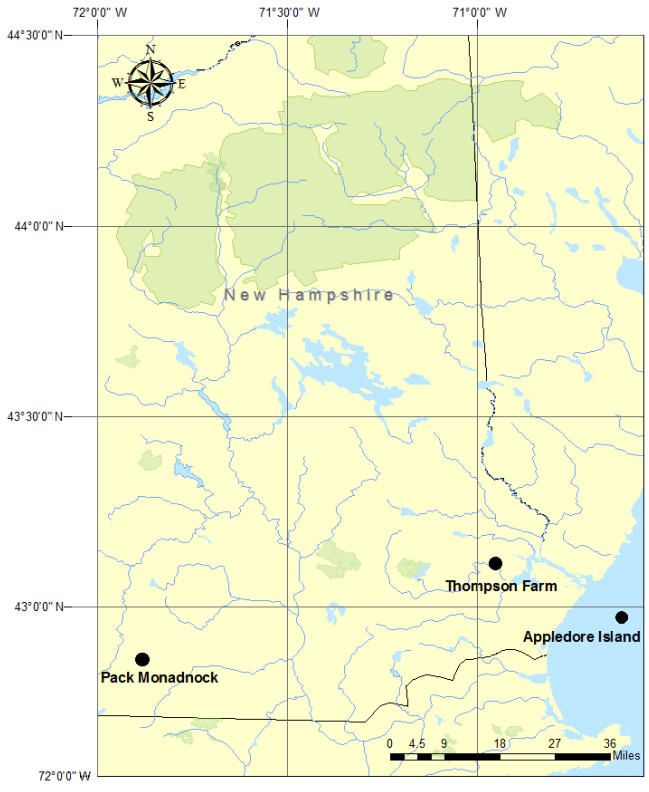

Figure 1. New Hampshire site map: Appledore Island (marine), Thompson Farm (coastal), and Pack Monadnock (inland elevated).

there was no temperature data available for summer 2009 at TF, 2009 was not considered.

2.3 Backward trajectory model

The National Oceanic and Atmospheric Administration (NOAA) Hybrid Single Particle Lagrangian Integrated Trajectory (HYSPLIT) trajectory model was used to identify source regions of air masses at the three sites. The model runs were performed over 24 h using the NOAA NAM (Eta) Data Assimilation System (EDAS) data with a 40 km × 40 km horizontal resolution as input. Backward trajectories and trajectory clusters were calculated.

2.4 Model evaluation

To evaluate the box model performance with observations, the following statistical performance measures (Chang and Hanna, 2004; Hanna, 1988; Hanna et al., 1991, 1993), which include the fractional bias (FB), the normalized mean square error (NMSE), the root mean square error (RMSE), and the partition of NMSE due to systematic errors ($NMSE_s$), were used:

$$FB = \left(\overline{C_0} - \overline{C_p}\right) / 0.5 \left(\overline{C_0} + \overline{C_p}\right), \quad (5)$$

$$NMSE = \overline{\left(C_0 - C_p\right)^2} / \overline{C_0 C_p}, \quad (6)$$

$$RMSE = \sqrt{\overline{\left(C_0 - C_p\right)^2}}, \quad (7)$$

$$NMSE_s = 4FB^2 / \left(4 - FB^2\right), \quad (8)$$

where C_p is model predictions, C_0 is observations, and overbar ($\overline{C}$) is the average over the dataset.

3 Results and discussion

3.1 General characteristics in measured GOM and GEM

In the 83 selected cases, atmospheric GOM and GEM mixing ratios varied greatly at the three sites (Fig. 2). Mixing ratios of GOM varied over 0.03–87.79 ppqv at AI, 0.04–4.93 ppqv at TF, and 0–0.65 ppqv at PM. At AI and TF, significant diurnal variation was observed with afternoon maximums and nighttime minimums. At AI, GOM peaked at 10 ppqv over 14:00–16:00 EDT and was ∼ 5 ppqv at night, well above the LOD (∼ 0.1 ppqv, from Sigler et al., 2009; the same LOD for the instruments at the three sites). At TF, GOM mixing ratios peaked at 0.75 ppqv at 17:00 EDT and were below LOD at night before 08:00 EDT. The GOM diurnal cycle at PM was different from that at AI and TF. At PM, averaged GOM had higher mixing ratios at night and in the early morning than in the afternoon. However, the median values showed afternoon peaks and nighttime minimums. The difference between average and median GOM diurnal cycles was driven by three cases that had abnormally high GOM mixing ratios (> 0.6 ppqv) at night or in the early morning relative to the average GOM mixing ratio during the day (∼ 0.1 ppqv).

Mixing ratios of GEM ranged over 65–231 ppqv at AI, 60–213 ppqv at TF, and 121–231 ppqv at PM (Fig. 2). On average, GEM mixing ratios at PM were 8 % higher than that at TF and 12 % higher than that at AI. Unlike GOM, GEM diurnal cycles showed nearly flat patterns at AI and PM, though slightly higher (∼ 3 %) GEM mixing ratios at night than in the daytime were observed at PM. In contrast, the average GEM diurnal cycle at TF showed an early morning (07:00 EDT) minimum (112 ppqv) and a daytime (13:00 EDT) maximum (153 ppqv).

The site differences of GOM and GEM diurnal cycles could be attributed to different chemical environments, land surface types, and meteorological conditions. For example, the GEM daily minimum at night and in the early morning at TF was likely caused by a strong net loss dominated by dry deposition under nocturnal inversion (Mao et al., 2008; Mao and Talbot, 2012). Nocturnal inversion also influenced the GEM and GOM diurnal cycles at PM, albeit differently from at TF. The elevation of the PM site is 700 m a.s.l., above the nocturnal inversion layer (< 200 m) (e.g., Kutsher et al.,

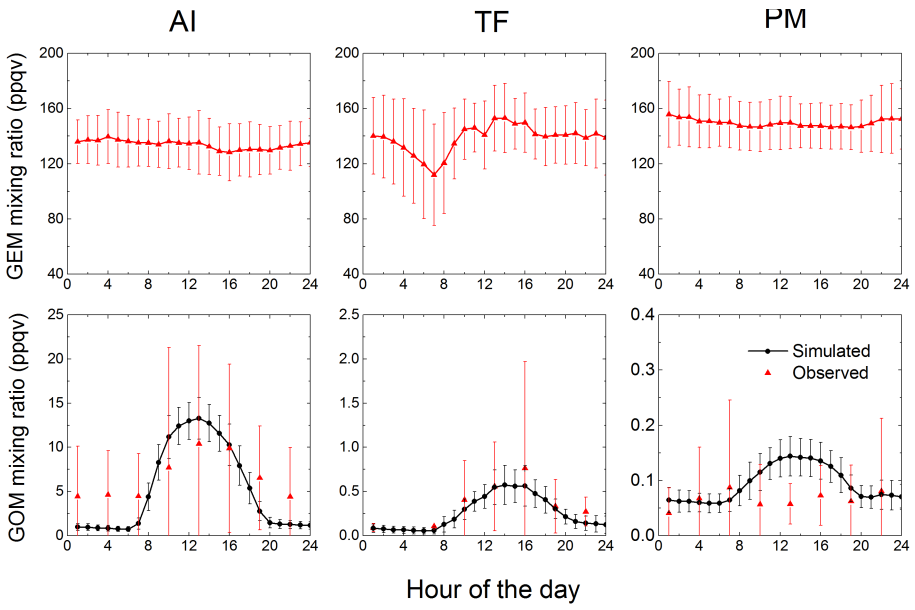

Figure 2. Average diurnal cycles of observed GEM (top panel) and simulated and observed GOM (bottom panel) averaged over the selected 50 days at Appledore Island (AI), 12 days at Thompson Farm (TF), and 21 days at Pack Monadnock (PM) from summers of 2007, 2008, and 2010. The error bars represent standard deviation.

2012), and thus GEM and GOM at night were continuously replenished by those produced from daytime and remaining in the residual layer, which likely caused higher nighttime values at PM. Daytime peaks of GOM at TF and AI were most likely caused by photochemical oxidation of GEM under strong solar radiation. The causes for such variation are examined in Sect. 3.4.2.

3.2 Simulated diurnal variation and speciation of GOM

Model simulated diurnal cycles of GOM averaged over the 50, 12, and 21 clear-sky days at AI, TF, and PM, respectively, were shown in Fig. 2. The patterns of diurnal variation were similar at the three sites, with a small discrepancy regarding the occurrence time of daily peaks ($\sim$ 13:00 LT at AI and $\sim$ 14:00 LT at TF and PM), but the magnitude varied greatly by site. AI had the largest GOM diurnal amplitude (i.e., daily maximum – daily minimum), ranging from 0.73 to 13.29 ppqv; TF varied from 0.05 to 0.57 ppqv, and PM showed a very small range from 0.05 to 0.14 ppqv. Similar magnitude variation was also exhibited in GOM observations (Fig. 2). Overall, simulated GOM mixing ratios at the three sites were in agreement with observations (detailed comparison in Sect. 3.3).

The simulations suggested that the dominant GOM species and GEM oxidants varied by site (Fig. 3). At AI, brominated GOM species comprised 59–81 % of the total GOM over 08:00–18:00 EDT, whereas HgO was dominant (50–92 % of the total GOM) during the remaining day. At TF and PM, HgO was the predominant GOM species (62–88 %). HgO was produced from the oxidation of GEM by O_3 and OH. The contribution to HgO from oxidation by O_3 was larger than by OH except at noon when OH mixing ratios reach daily peaks, resulting in comparable contributions (48 and 52 % by OH and O_3, respectively). At AI, $BrHgNO_2$ and HgBrO were the most abundant brominated GOM species, which constituted $\sim$ 96 % of the total brominated GOM. HgBrO was produced from the GEM + BrO reaction, while $BrHgNO_2$ was produced from GEM oxidation by Br radicals followed by reactions of HgBr with NO_2. $Hg(OH)_2$ from GEM oxidation by H_2O_2 appeared to be an important nighttime GOM species at the inland site (PM), accounting for 33 % of the total GOM at night. Other GOM species were negligible in the studied cases.

3.3 Model evaluation

For all cases at AI and TF, the average simulated and observed GOM diurnal cycles agreed reasonably well in both magnitude and shape, whereas at PM the model appeared to have missed both (Fig. 2). Three salient features were noted for the disagreement between the model and observational results. First, the standard deviation of observed GOM mixing ratios was a factor of 2–7 larger than that of the simulated ratios. This suggested that the model could capture the mean values of GOM but not the very low and very large mixing ratios. Second, observed nighttime GOM mixing ratios were 12–200 % larger than those simulated at AI, indicating that the model did not capture certain nighttime processes producing GOM in the MBL. Third, the simulated diurnal cycle was the opposite of the observed cycle at PM, with the max-

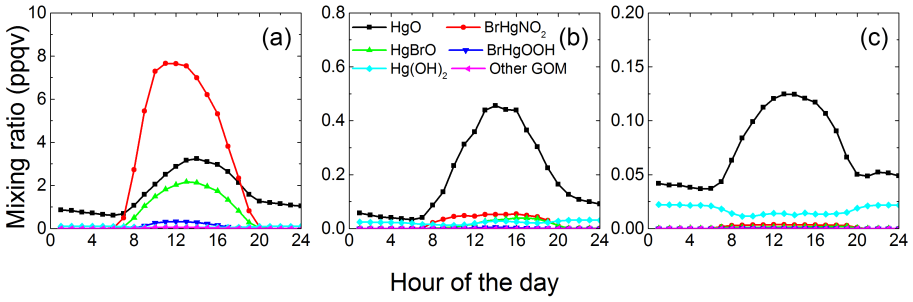

Figure 3. Simulated average diurnal cycles of GOM speciation at AI **(a)**, TF **(b)**, and PM **(c)**.

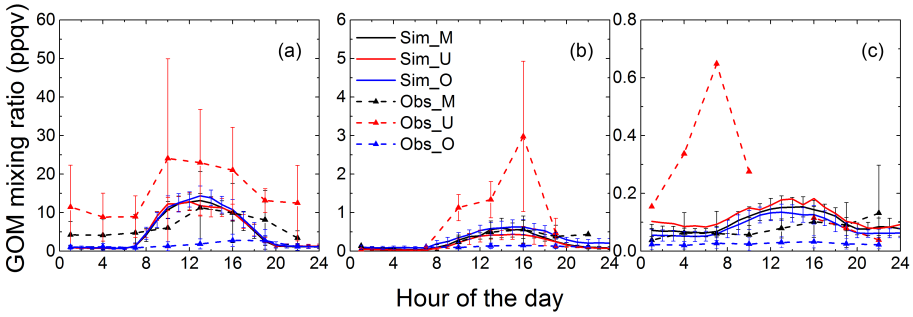

Figure 4. Observed (dash line with scatters) and simulated (solid line) average diurnal cycles of GOM for the matching (black, "Sim_M" and "Obs_M"), underestimation (red, "Sim_U" and "Obs_U"), and overestimation cases (blue, "Sim_O" and "Obs_O") at AI **(a)**, TF **(b)**, and PM **(c)**. The bars represent the standard deviations at each hour for those specific days.

imum during the day and the minimum at night. It was likely that the model simply simulated the dependence of GOM production on solar radiation. At PM, more processes may have contributed to the diurnal variation. At night, the site is above the nocturnal boundary layer and exposed to the GOM produced in the preceding convective boundary layer, which could continually replenish surface GOM at the site that was lost via dry deposition and perhaps reduction. The model–observation discrepancies of GOM at the three sites are discussed in what follows.

3.3.1 Appledore Island (marine)

Of the 50 cases at AI, 27 diurnal cycles of GOM were simulated with the average values and patterns close to those observed, with $NMSE_s = 1.88\,\%$, denoted as *matching* cases hereafter; 8 were underestimated, with $NMSE_s = 121\,\%$; and 15 were overestimated, with $NMSE_s = 171\,\%$. The observed and simulated average GOM mixing ratios and the corresponding ranges were calculated for the matching, underestimation, and overestimation cases at AI (Fig. 4a). For more than half of the time (27 matching cases out of 50 cases in total), the model captured the average GOM diurnal cycle, the diurnal cycle pattern, and overall GOM levels. Beyond that, Fig. 4a shows a large difference in the observed GOM levels among the matching, underestimation, and overestimation cases. On average, the observed daytime peak in the underestimation cases was about twice as large as that for the matching cases and 7 times larger than that for the overestimation cases. However, such a difference was not captured by the model, suggesting that some GOM-producing processes in the MBL were not included or not realistically represented in the box model. In addition, the GOM diurnal pattern in the overestimation cases was different from those in the underestimation and matching cases. The average observed GOM diurnal cycles of the underestimation and matching cases both exhibited a daily maximum at 13:00 EDT and a minimum over 04:00–08:00 EDT, whereas the overestimation cases showed a daily maximum at around 20:00 EDT and a minimum at 07:00–08:00 EDT.

Such differences were due possibly to the challenges of simulating Br and BrO in the MBL at AI. No measurements of Br and BrO radicals or of Br_2 were available at AI. To reasonably simulate mixing ratios of Br and BrO, Br_2 mixing ratios were calculated based on the BrO observations at a midlatitude MBL site from Saiz-Lopez et al. (2006), which was ~ 5.6 ppqv during the daytime (06:00–21:00 EDT). Saiz-Lopez et al. (2006) showed that daytime peak mixing ratios of BrO in the MBL could vary by a factor of 2 over a time period of 3 days. Such variation was not captured in our box model, potentially resulting in uncertainty of up to 100 % in simulated Br mixing ratios with subsequent effects on GOM simulation.

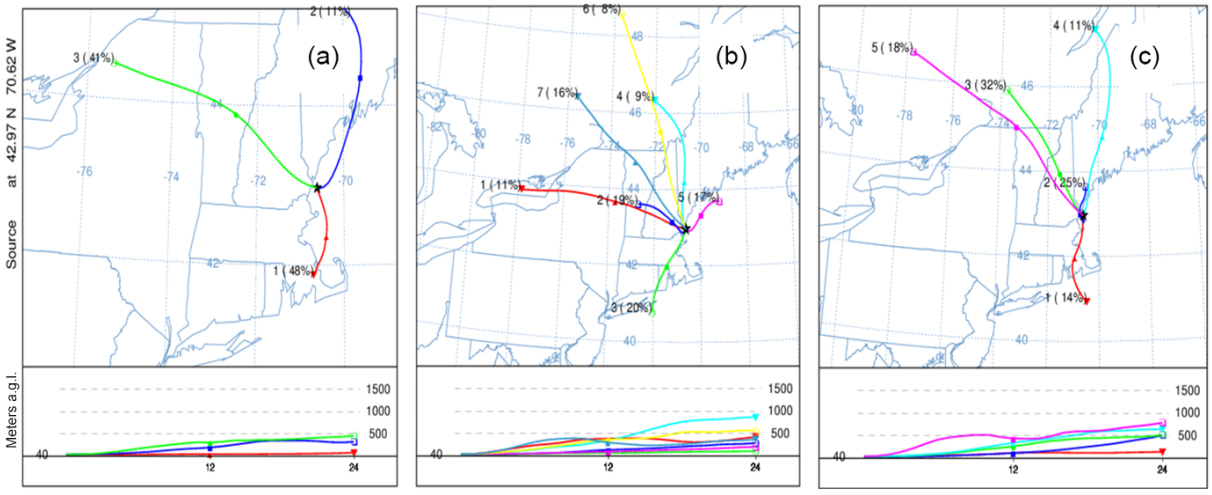

Figure 5. Clustered 24 h back trajectories of air masses in **(a)** overestimation cases, **(b)** matching cases, and **(c)** underestimation cases at AI.

In the overestimation cases, the simulated GOM daytime peaks were very low and appeared later during the day than in the underestimation and matching cases. Considering the late afternoon peak (17:00 EDT) of O_3 compared to the noontime peak of Br radicals, O_3 possibly played a more important role in the overestimation cases. To verify this hypothesis, a sensitivity simulation was conducted without the initial Br_2 mixing ratio fixed for these cases, termed the O_3/OH scenario. In these sensitivity runs, the Br_2 concentration rapidly diminished with time, leading to very low concentrations of Br and BrO. The O_3/OH scenario turned out to better represent these 15 overestimation cases, with $NMSE_s = 34\,\%$ (compared to 167 % with the Br_2 mixing ratio fixed).

These sensitivity simulations suggested that in the MBL, Br may be dominant in GEM oxidation most of the time, but at times of low Br mixing ratios, O_3 could become dominant. To identify the origin of the air masses at AI, backward trajectory analysis was conducted using the HYSPLIT4 model (https://ready.arl.noaa.gov/HYSPLIT.php). All 24 h backward trajectories started from the time of GOM daily peaks for the 50 cases. The trajectory results were clustered for overestimation, matching, and underestimation cases (Fig. 5). Based on these trajectories, in about half of the 15 overestimation cases air masses originated from marine environments, while in more than 80 % of the 27 matching cases and 7 out of 8 underestimation cases air masses came from inland, northwest of AI. Note that in these underestimation cases, GOM mixing ratios were exceptionally large, exceeding 30 ppqv.

Different source areas of air masses reaching AI could be one of the reasons for the large variation in GOM observations. The highest levels of GOM were observed in summer, with RH roughly $< 50\,\%$ at AI (Mao et al., 2012). A close examination of the 50 cases at AI revealed low RH levels ($\leq 45\,\%$) on 16 days. The time periods with RH $\leq 45\,\%$ appeared mostly (78 % of the time) in the afternoon over 12:00–20:00 EDT and less so (22 %) at night over 21:00–02:00 EDT. During these time periods, increased GOM (15 out of 16, compared with periods with high RH on the same day) and daily maximum GOM (10 out of 16) occurred simultaneously at low RH, regardless of the time of the day.

Interestingly, the RH level of 45 % corresponds to the crystallization point of NaCl (Cziczo et al., 1997; Tang et al., 1997). The crystallization of sea salt aerosols may be linked to the very high GOM peaks in certain ways. Rutter and Schauer (2007) found that particles of potassium and sodium chlorides had high partitioning coefficients that could shift the GOM gas–particle partitioning toward the aqueous phase, while ammonium sulfate, levoglucosan, and adipic acid would shift the partitioning toward the gas phase. It was thus hypothesized that, when these inland air masses reached the MBL mixed with the marine air, the processes discussed above may have been activated involving the interaction between land and marine air, which potentially resulted in those very high GOM mixing ratios.

Laskin et al. (2012) found effective reactivity of chloride (Cl^-) components with organic acid in sea salt aerosols (SSAs), possibly leading to the depletion of Cl^- and formation of organic salts in aerosols. Biogenic compounds in air masses originating from inland forested areas could be oxidized forming organic acids in transit. As inland air reached the MBL, these organic acids would deposit onto SSAs and could subsequently change SSAs' chemical and physical properties, such as lowering concentrations of Cl^- and forming a thick organic film on the outside of SSAs. The lower concentrations of Cl^- and higher concentrations of organic acid in aerosols may have contributed to the shift in the gas-to-particle partitioning to the gas phase and resulted in higher GOM mixing ratios in the atmosphere.

Another possible explanation could be air masses of inland origin encountering marine air rich in atmospheric Br and BrO radicals. The main source of atmospheric Br is

thought to come from the release of Br_2 and BrCl from SSA (Finlayson-Pitts, 2010; Sander et al., 2003). Experimental studies suggested Br^- enhancements of a factor of 40 to 140 on the surface of sufficiently dry artificial SSA (Ghosal et al., 2008; Hess et al., 2007). Therefore, when drier inland air masses were mixed with marine air in the MBL under relatively low RH conditions, SSA became drier, forcing more Br_2 to be released from SSA, resulting in enhanced oxidation of GEM by Br and BrO radicals. These hypotheses need to be validated in future research. These mechanisms are presently missing in the box model, leading to the model's inability to capture very high GOM mixing ratios. Measurements of halogen species and a better gas–particle partitioning mechanism are needed to better the model's performance.

3.3.2 Thompson Farm (coastal)

Generally, the box model performed well at TF (Fig. 2), with overall $NMSE_s = 0.75\,\%$ and $RMSE = 0.78$ ppqv. Of the 12 cases at TF, 6 diurnal cycles of GOM (50 %) were simulated reasonably well, with $NMSE_s < 50\,\%$, 2 were underestimated by $\sim 70\,\%$, and 4 cases were overestimated by a factor of 2 to 5. Overall, the observed average diurnal cycles of GOM for all selected summer clear-sky days at TF had daily peaks during 14:00–20:00 EDT with very low values at night between 00:00 and 08:00 EDT (Sigler et al., 2009) (Fig. 2). The peak observed at 17:00 EDT (Fig. 2) was largely affected by the abnormally high GOM peak in that one underestimation case (Fig. 4b).

For the overestimation and matching cases, the model reproduced very low GOM mixing ratios at night (Fig. 4b). The low nighttime GOM at TF was probably caused by loss via dry deposition under nocturnal inversion, and it substantially lowered GEM mixing ratios at night and in the early morning at TF for the same reason (Mao et al., 2008). To capture these low values in model simulations, realistic nocturnal boundary layer height data were needed beside a solid representation of dry deposition and chemistry in the model. The diurnal cycle of boundary layer height in the box model was parameterized based on reanalysis data obtained from the Research Data Archive at the National Center for Atmospheric Research (http://rda.ucar.edu/datasets/ds093.0/). Use of these data helped to reproduce the low nighttime GOM levels in simulations for the TF site. Another notable feature in Fig. 4b is the exceedingly high observed GOM mixing ratios in the underestimation cases and the low observed GOM mixing ratios throughout the day in all overestimation cases. Observed GOM mixing ratios in the underestimation cases were a factor of 3–4 larger than those in the matching cases and a factor of 3–31 larger than those in the overestimation cases (Fig. 4b). Concurrently, larger fine-particle concentrations, 7468 cm^{-3} on average, were observed for the underestimation cases, which was 51 and 80 % larger than those in the matching cases and overestimation cases, respectively. Lower RH, 66 % on average, was observed in the underestimation cases, 5 and 11 % lower than that in the matching and overestimation cases, respectively. Moreover, higher air pressure (1018 hPa; 8 and 12 hPa larger than the matching and overestimation cases, respectively), lower wind speed (0.8 m s^{-1} on average, 35 and 68 % lower than matching and overestimation cases respectively), and stronger solar radiation flux (8 and 13 % stronger than matching and overestimation cases respectively) were found in the underestimation cases. An examination of the sea level pressure maps (Fig. S1) in the underestimation cases suggested that these cases occurred under the strongest Bermuda High influence, with the calmest, sunniest, and driest conditions of all cases, which is most conducive to photochemistry and pollution buildup and may have ultimately contributed to the very large GOM mixing ratios in those underestimation cases. Our model appeared to fail to mimic the chemistry under such conditions that produced the largest GOM mixing ratios.

3.3.3 Pack Monadnock (inland, rural, elevated site)

At PM, diurnal cycles of GOM were overestimated, with $NMSE_s = 70\,\%$ and overall $RMSE = 0.13$ ppqv. However, considering the extremely low mixing ratios of GOM observed at PM (Fig. 2), cases with $RMSE < 0.1$ ppqv (LOD) were considered to be matching cases. Therefore, the model reasonably simulated 11 out of 21 (52 %) cases, underestimated in 1, and overestimated in 9. Evaluation of simulated GOM diurnal cycles against observations (Fig. 2) showed reasonable agreement with general overestimation, ranging over 0.05–0.07 ppqv.

The observed GOM diurnal cycle (Fig. 2f) showed daily maximums at 08:00 and 23:00 EDT, which were mainly influenced by the underestimated case (Fig. 4c). In comparison, the remaining (95 %) cases showed a very flat GOM diurnal cycle at PM. The first and most important reason for such observation–model discrepancy is that the PM site is a mountain site (700 m a.s.l.), which is above the nocturnal inversion layer (~ 200 m at TF) but within the convective boundary layer during the day. At night, a regional pool of GOM produced in the preceding convective boundary layer remained in the residual layer, which kept the surface GOM levels from dropping below the LOD at night at PM. The slight decline in GOM mixing ratios after sunrise was because of mixing with the lower-altitude air masses with depleted GOM from the night. The effect of PM's site characteristics was not represented in the box model, which could result in model's inability to simulate diurnal variation associated with this aspect of the site. In addition, due to the dominance of GEM oxidation by O_3 in GOM production in the model, it was highly likely that the flat diurnal cycles (slightly higher at night) of GEM (Fig. 2) and O_3 were mirrored in GOM mixing ratios.

Table 3. Sensitivity scenarios with varying physical and chemical parameters. The superscript D represents daytime and N nighttime. Downward arrows stand for decreases and upward arrows for increases. T stands for the temperature diurnal cycle in the base scenario, and $T + 10$ K or $T - 10$ K represents a 10 K higher temperature or a 10 K lower temperature throughout the day, respectively.

Scenario no.	Photolysis	Gas–droplet partitioning		Rate coefficients (cm^3 $molec^{-1}$ s^{-1})			Temp.	Results	
		Included	Liquid water content (m^3_{water} m^{-3}_{air})	GEM + O_3 (298 K)	GEM + OH (298 K)	GEM + Br (298 K)		GOM	PBM
Base scenario									
0	Yes	Yes	5.0×10^{-11}	$7.5\times10^{-19,a}$	$9.5\times10^{-14,b}$	$3.7\times10^{-13,c}$	T	–	–
Photochemistry									
1	No	Yes	5.0×10^{-11}	7.5×10^{-19}	9.5×10^{-14}	3.7×10^{-13}	T	↓ 3–92 %^{D}	↓ 2–100 %^{D}
Gas–particle partitioning									
2	Yes	No	–	7.5×10^{-19}	9.5×10^{-14}	3.7×10^{-13}	T	↑∼ 280 %	↓ 100 %
Liquid water content									
3	Yes	Yes	3.0×10^{-12}	7.5×10^{-19}	9.5×10^{-14}	3.7×10^{-13}	T	↑∼ 200 %	↓ 80 %
4	Yes	Yes	3.0×10^{-10}	7.5×10^{-19}	9.5×10^{-14}	3.7×10^{-13}	T	↓ 80 %	↑ 50 %
Reactions									
5	Yes	Yes	5.0×10^{-11}	$3.0\times10^{-20,d}$	9.5×10^{-14}	3.7×10^{-13}	T	↓ 15 %^{D} ↓ 85 %^{N}	↓ 49 %^{N}
6	Yes	Yes	5.0×10^{-11}	–	9.5×10^{-14}	3.7×10^{-13}	T	↓ 16 %^{D} ↓ 88 %^{N}	↓ 51 %^{N}
7	Yes	Yes	5.0×10^{-11}	7.5×10^{-19}	–	3.7×10^{-13}	T	↓ 10 %^{D}	Negligible
8	Yes	Yes	5.0×10^{-11}	7.5×10^{-19}	9.5×10^{-14}	–	T	↓ 48 %^{D}	↓ 60 %^{D}
9	Yes	Yes	5.0×10^{-11}	7.5×10^{-19}	9.5×10^{-14}	$3.2\times10^{-12,e}$	T	↑ 250 %^{D}	↑ 300 %
Temperature									
10	Yes	Yes	5.0×10^{-11}	7.5×10^{-19}	9.5×10^{-14}	3.7×10^{-13}	$T + 10$ K	↓ 9 %^{D} ↑ 13 %^{N}	↓ 9 %^{D} ↑ 54 %^{N}
11	Yes	Yes	5.0×10^{-11}	7.5×10^{-19}	9.5×10^{-14}	3.7×10^{-13}	$T - 10$ K	↑ 9 %^{D} ↓ 11 % ^{N}	↑ 8 %^{D} ↓ 28 %^{N}

[a] Snider et al. (2008); [b] Pal and Ariya (2004a); [c] Goodsite et al. (2004, 2012); [d] Hall (1995); [e] Ariya et al. (2002).

3.4 Sensitivity analysis

3.4.1 Sensitivity of GOM to physical and chemical parameters

The base scenario (Scenario 0) of these sensitivity runs represented the real atmospheric conditions on the selected 50 days at AI. Scenarios 1–10 are sensitivity runs where one parameter in the base scenario was changed at the time (Table 3). Scenario 1 turned off photolysis reactions. Scenarios 2–4 tested the gas–particle partitioning scheme. The liquid water content range was derived from Hedgecock et al. (2003). Scenarios 5–9 tested the sensitivity of GOM mixing ratios to GEM oxidation reactions and their coefficients. Scenarios 10–11 tested the sensitivity of GOM mixing ratios to temperature. The temperature range was based on the observed average temperature diurnal cycle.

The importance of photochemical radicals in GEM oxidation was demonstrated clearly in decreases of 3–92 and 2–100 % in daytime GOM and PBM, respectively, with largest decreases at noon as a result of turning off photochemistry (Scenario 1). Scenario 2 showed ∼ 74 % of oxidized Hg transformed to PBM at AI with gas–particle partitioning switched on. In this scenario, HgO and $Hg(OH)_2$ were more sensitive than halogenated GOM species (such as $BrHgNO_2$). Turning off gas–particle partitioning more than quadrupled the mixing ratios of HgO and $Hg(OH)_2$ throughout the day compared to increases of more than 100 and 60 % halogenated GOM species during daytime and nighttime, respectively.

Decreasing liquid water content by 1 order of magnitude tripled GOM mixing ratios, whereas increasing the same amount decreased GOM by 80 % (Scenarios 3–4). The sensitivity of GOM and PBM mixing ratios to dominant GEM oxidation reactions is shown in Scenarios 5–9. Using the slowest rate coefficient of GEM + O_3 obtained from Hall (1995), as opposed to the one from Snider et al. (2008), led to a decrease of 56.7 % in HgO and decreases of 15 and 85 % in total GOM during daytime and nighttime, respectively. Using a rate coefficient of GEM + Br from Ariya et al. (2002) that is an order of magnitude faster increased total GOM during daytime by 250 %. Turning off GEM oxidation by O_3, OH, or Br resulted in decreases of 16, 10, and 48 %, respectively, in daytime GOM mixing ratios. Turning off the GEM + Br oxidation reaction also decreased daytime PBM mixing ratios by 60 %. However, for nighttime GOM and PBM mixing ratios, turning off the GEM + O_3 reaction caused decreases of 88 and 51 %, respectively, since Br and OH are both photochemical radicals and O_3 was the predominant oxidant for GEM in the model.

Scenarios 10–11 suggested that nighttime GOM and PBM mixing ratios were more sensitive to temperature than those during daytime. Increasing temperature by 10 K caused a 9 % increase in both GOM and PBM mixing ratios during daytime but a decrease of 13 % in GOM and 54 % in PBM at night. This was because the rate coefficient of GEM + O_3 increases with increasing temperature, but the rate coefficient of GEM + OH decreases with increasing temperature.

In summary, the parameters used in the gas–particle partitioning process, including solar radiation values, temperature, and the rate coefficients of major GEM oxidation reaction, could all affect the GOM simulation but to varying degrees. Aerosol properties were suggested to play a very important role in the partitioning of ambient GOM and PBM species and thus should be better represented in future Hg model simulation studies. Using a slower rate coefficient of GEM + O_3 (Hall, 1995) had similar effects to not including the GEM + O_3 reaction, i.e., decreasing GOM mixing ratios, especially at nighttime, and brominated GOM species becoming dominant. The GEM + OH reaction was not as important as GEM + O_3 or Br. The use of a higher GEM + Br rate coefficient derived from the study by Ariya et al. (2002) caused GOM and PBM that were more than a factor of 3 higher, resulting in overestimated GOM for most cases. GOM and PBM production appeared to favor lower temperature at daytime and higher temperature at night, and simulated GOM concentrations were not as sensitive to temperature change as to solar radiation and gas–particle partitioning.

3.4.2 Influence of physical and chemical processes on GOM diurnal cycle

Large variations were exhibited in both observed and simulated GOM mixing ratios at AI, TF, and PM (Fig. 2). Considering that all cases were under relatively calm, clear-sky conditions, the simulated GOM mixing ratio and diurnal cycle were controlled primarily by chemical reactions, dry deposition, and gas–particle partitioning. To quantify the contribution of processes to the difference of GOM mixing ratios at the three sites, two sensitivity scenarios were conducted using the same physical parameters as those of AI for TF (denoted as TF_AIaerodry) and PM (denoted as PM_AIaerodry).

Comparison of simulated GOM diurnal cycles from the AI, TF_AIaerodry, and PM_AIaerodry scenarios showed the influence of different chemical scenarios on GOM mixing ratios at the three sites. At night, GOM mixing ratios at the three sites did not vary significantly (0–2 ppqv), with higher values at PM than at AI and TF (Fig. 6). However, the midday peak at AI was more than a factor of 2 greater than those in the PM_AIaerodry and TF_AIaerodry scenarios, indicating more chemical transformation of Hg occurring at AI. The daytime mixing ratios of GOM at TF and PM were similar, while the nighttime GOM mixing ratios at PM were 30–52 % higher than at AI and 20–200 % higher than at TF. This probably resulted from larger nighttime GEM and O_3 mixing ratios, hence producing more GOM, at PM than at TF and AI. Specifically, nighttime GEM mixing ratios at PM were 8–15 % higher than at AI and 8–34 % higher than TF cases, while nighttime O_3 mixing ratios at PM were 11–70 % larger than at AI and 35–260 % larger than at TF. PM had higher nighttime GEM and O_3 mixing ratios because this site was exposed in the residual boundary layer at night due to its high elevation and was constantly replenished with the regional pool of air from the preceding convective boundary layer. Overall, chemical transformation contributed ∼ 60 % of the daytime difference in GOM between AI and the two sites over land (TF and PM), 33 % of the nighttime difference between AI and TF, and 26 % of the difference between PM and AI.

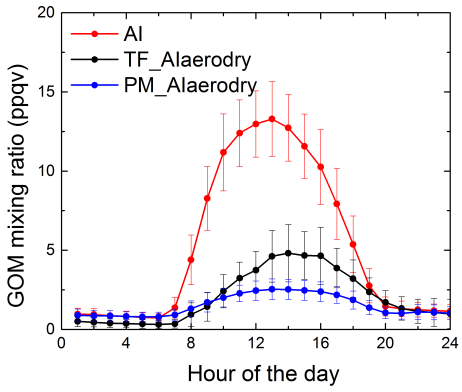

Figure 6. Simulated averaged diurnal cycles of GOM at AI (red), at TF (black) using AI dry deposition and gas–aerosol partitioning parameters ("TF_AIaerodry"), and at PM (blue) using AI dry deposition and gas-to-particle partitioning parameters ("PM_AIaerodry").

In summary, the sensitivity scenarios suggested that dry deposition and gas–particle partitioning contributed 4–37 % and 30–96 %, respectively, of the total GOM difference between AI and PM. Both processes had larger contributions at night that during daytime. Dry deposition contributed 6–24 % of the GOM difference between AI and TF and gas–particle partitioning 18–78 %.

3.4.3 Br chemistry in the MBL

Diurnal cycles of Br and BrO radicals (Fig. 7) were simulated using the Br chemical mechanism described in Sect. 2. Photodissociation of Br_2 was the main source of Br and BrO radicals during daytime. Our simulations suggested that reactive Br compounds were significant gaseous oxidants of GEM in the MBL at a fixed initial mixing ratio of 5.6 ppqv for Br_2. Increasing initial mixing ratios of Br_2 by 25 % resulted in an increase of 0.01–2.15 ppqv in GOM mixing ratios.

Table 4. Possible pathways of $BrO + CH_3O_2$ reaction.

No.	Reactions	Kinetics (cm^3 $molecule^{-1}$ s^{-1})	Reference
B1	$BrO(g) + CH_3O_2(g) \rightarrow CH_3O(g) + BrOO(g)$ $BrOO(g) \rightarrow Br(g) + O_2(g)$	1.4×10^{-12} Fast	Aranda et al. (1997), Atkinson et al. (2008)
B2	$BrO(g) + CH_3O_2(g) \rightarrow CH_2O_2(g) + HOBr(g)$	4.3×10^{-12}	Aranda et al. (1997), Atkinson et al. (2008)
B3	$BrO(g) + CH_3O_2(g) \rightarrow CH_3OBr(g) + O_2(g)$	?	Aranda et al. (1997)
B4	$BrO(g) + CH_3O_2(g) \rightarrow CH_3OOOBr(g) \rightarrow$ $CH_2O(g) + HOOBr(g)$	?	Guha and Francisco (2003)

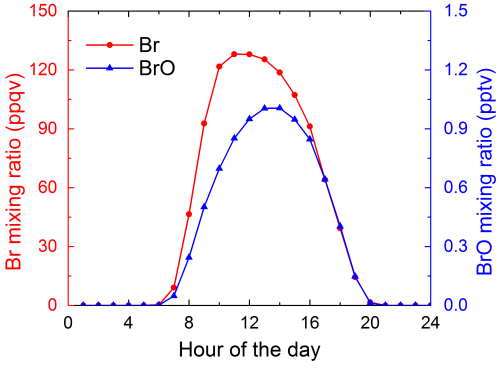

Figure 7. Simulated diurnal cycles of Br (red) and BrO (blue) of the base case.

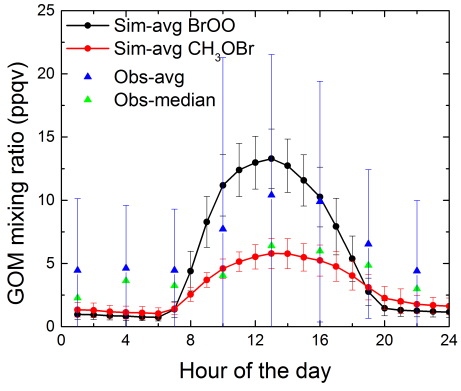

Figure 8. Simulated average diurnal cycles of GOM for the base scenario ("Sim-avg BrOO", black circle) and for the "CH_3OBr" scenario ("Sim-avg CH_3OBr", red, circle), observed average GOM diurnal cycle ("Obs-avg", blue, triangle scatter), and observed median GOM diurnal cycle ("Obs-median", green, triangle scatter) of the 50 cases at AI.

In addition, the reaction of BrO with methyldioxy (CH_3O_2) radicals could have an important influence on the mixing ratios of Br, BrO, and GOM. The simulated daytime mixing ratio of CH_3O_2 was ~ 40 pptv, and the rate coefficient of $(5.7 \pm 0.6) \times 10^{-12}$ cm^3 $molecule^{-1}$ s^{-1} at 298 K for $BrO + CH_3O_2$ (Aranda et al., 1997) was used for our simulations. Pathways B1, B2, and B3 were suggested by Aranda et al. (1997) based on an experimental study (Table 4). However, the production of CH_3O may be due to its self-reaction in B1. Guha and Francisco (2003) suggested CH_3OOOBr to be a likely intermediate of this reaction and that CH_3OOOBr could dissociate to $CH_2O + HOOBr$ (B4, Table 4). Based on thermodynamics calculations, CH_3OBr and O_2 (B3, Table 4) were possible products. BrOO and HOBr were both included in the Br chemical cycle and can be transformed back to Br and BrO radicals in the model. However, it is unclear whether CH_3OBr (product of B3) or HOOBr (product of B4) could be transformed back to Br and BrO radicals in the atmosphere. In this case, using the B3 or B4 pathway did not appear to make a difference in our box model results.

In this study, the B1 and B2 pathways were used for the $CH_3O_2 + BrO$ reaction as part of the base scenario (denoted as Sim-avg BrOO). The sensitivity run Sim-avg CH_3OBr used the B3 pathway in lieu of B1 and B2. The simulated average and the range of GOM diurnal cycles in the base and sensitivity scenarios were evaluated against observed mean and median GOM diurnal cycles of the 50 study cases at AI (Fig. 8). If the $CH_3O_2 + BrO$ reaction followed the B1 and B2 pathways, this reaction had a negligible effect on reactive Br radicals. However, if B3 or B4 was applied, the simulated total GOM mixing ratio was lowered by 50 % during daytime. Moreover, the simulated GOM diurnal cycle in the base scenario agreed favorably with the observed average GOM diurnal cycle (NMSE = 15 %), while the results of the Sim-avg CH_3OBr scenario were in better agreement with the observed median GOM diurnal cycle (NMSE = 14 %). These agreements indicated that, if the $BrO + CH_3O_2$ reaction was a net sink of BrO radicals, the model was able to simulate most cases better, whereas if the product of $BrO + CH_3O_2$ was transformed back to Br or BrO radicals, the model appeared to capture those cases with large GOM mixing ratios (> 6 ppqv). Due to the scarcity of kinetic research on the B3 and B4 pathways, we used B1 and B2 pathways for $CH_3O_2 + BrO$ reaction in this study.

In short, the pathways of $BrO + CH_3O_2$ could play an important role in atmospheric Br chemistry and Hg speciation

in Br-rich environments. Research on the reaction pathways and rate coefficients of the $BrO + CH_3O_2$ reaction is warranted to better assess the role of this reaction.

4 Summary

This study provided a state-of-the-art chemical mechanism with most up-to-date Hg and halogen chemistry and tested the mechanism for three different environments using a mercury box model. Eighty-three summer clear-sky days were selected at marine, coastal, and inland elevated sites in southern New Hampshire to evaluate the model. As a result, for each of the three environments, GOM diurnal cycles of over half of the selected cases were reasonably represented by the box model. It was hypothesized, based on the key results and discussion presented in Sect. 3, that dry air masses with organic compounds transported from inland may result in very large GOM mixing ratios in the MBL, possibly due to changing physical and chemical properties of sea salt aerosols. The low nighttime and morning GOM mixing ratios at a coastal site were likely a result of a net loss due to dry deposition in the nocturnal inversion layer. The GOM mixing ratios above the LOD at the inland site at night were probably caused by constant replenishment from a regional pool, in the residual boundary layer, of GOM that was produced in the preceding daytime convective boundary layer. The updated chemical mechanism largely improved the simulation of the magnitude and pattern of GOM diurnal variation at the coastal and inland sites. HgO produced from oxidation of GEM by O_3 and OH dominated GOM species at the coastal and inland sites, while bromine-induced mercury species (mainly BrHgOOH, BrHgOBr, and HgBrO) were important at the marine site. In Br chemistry, the products of the $CH_3O_2 + BrO$ reaction strongly influenced the simulated Br and Hg concentrations. In this study, GEM oxidation by O_3 and OH was represented in ways similar to those in regional and global models, which is limited by the current nebulous understanding of potential surface chemistry.

It should be noted that without measurements of speciated GOM, modeling results cannot be used to conclusively identify the dominant oxidants of Hg, as well as dominant GOM species for that matter, in the atmosphere. Indeed, the potential uncertainty in ambient Hg measurements, especially GOM, is a major concern in the community. That being said, the community is unlikely to have a quantitative understanding of the bias of our GOM concentrations. Recent laboratory experiments and reviews (Lyman et al., 2010; Jaffe et al., 2014; McClure et al., 2014; Huang and Gustin, 2015; Gustin et al., 2015) reported O_3 and relative humidity (RH) interferences on mercury halides for a KCl-coated denuder, the part of the Tekran 1130 unit commonly used for GOM field measurements. As stated in Sect. 2, in our GOM measurement the RH effect was minimized by adding refrigeration to remove excess water from the airstream. O_3 interference and low-bias GOM collection efficiency of KCl-coated denuders were limited to a handful of GOM species in laboratory experiments and remain untested in field measurements. If the measured GOM concentrations were indeed biased low by a factor of 2 or 3 under certain conditions as previous studies speculated, the matching cases at AI and TF would be reduced from 50 % of the total cases to 30 % and the model would potentially underestimate GOM concentrations in the remaining cases (70 %) by a factor of 3 to 4. It is, however, hard to speculate on the effect at PM since most GOM observations there were below the LOD. This suggested even greater unknowns in our understanding of Hg chemistry. Therefore, more experimental or theoretical studies on Hg reactions and better GOM measurement data are warranted to improve our understanding and subsequently model simulations of atmospheric Hg cycling, which can ultimately serve policy making in an effective manner.

5 Data availability

The model data used in this study are available on request to Huiting Mao. The observational data are also available at http://www.eos.unh.edu/observatories/data.shtml (University of New Hampshire, 2016).

The Supplement related to this article is available online at doi:10.5194/acp-16-8461-2016-supplement.

Acknowledgements. This work is funded by NSF AGS grant no. 1141713. We thank T. Dibble, Y. Zhou, Y. Zhang, and C. B. Hall for valuable suggestions and help. We are grateful to the three anonymous reviewers for their thoughtful, detailed, constructive comments, which helped to improve the clarity of the paper.

Edited by: L. Zhang

References

Aranda, A., Le Bras, G., La Verdet, G., and Poulet, G.: The $BrO + CH_3O_2$ reaction: kinetics and role in the atmospheric ozone budget, Geophys. Res. Lett., 24, 2745–2748, 1997.

Ariya, P. A., Khalizov, A., and Gidas, A.: Reactions of gaseous mercury with atomic and molecular halogens: kinetics, product studies, and atmospheric implications, J. Phys. Chem. A, 106, 7310–7320, 2002.

Ariya, P. A., Amyot, M., Dastoor, A., Deeds, D., Feinberg, A., Kos, G., Poulain, A., Ryjkov, A., Semeniuk, K., Subir, M., and Toyota, K.: Mercury physicochemical and biogeochemical transformation in the atmosphere and at atmospheric interfaces: a review and future directions, Chem. Rev., 115, 3760–3802, doi:10.1021/cr500667e, 2015.

Atkinson, R., Baulch, D. L., Cox, R. A., Crowley, J. N., Hampson, R. F., Hynes, R. G., Jenkin, M. E., Rossi, M. J., and Troe, J.: Evaluated kinetic and photochemical data for atmospheric chemistry: Volume I – gas phase reactions of O_x, HO_x, NO_x and SO_x species, Atmos. Chem. Phys., 4, 1461–1738, doi:10.5194/acp-4-1461-2004, 2004.

Atkinson, R., Baulch, D. L., Cox, R. A., Crowley, J. N., Hampson, R. F., Hynes, R. G., Jenkin, M. E., Rossi, M. J., Troe, J., and Wallington, T. J.: Evaluated kinetic and photochemical data for atmospheric chemistry: Volume IV – gas phase reactions of organic halogen species, Atmos. Chem. Phys., 8, 4141–4496, doi:10.5194/acp-8-4141-2008, 2008.

Balabanov, N. B., Shepler, B. C., and Peterson, K. A.: Accurate global potential energy surface and reaction dynamics for the ground state of $HgBr_2$, J. Phys. Chem. A, 109, 8765–8773, 2005.

Baumgardner, D., Raga, G. B., Kok, G., Ogren, J., Rosas, I., Báez, A., and Novakov, T.: On the evolution of aerosol properties at a mountain site above Mexico City, J. Geophys. Res.-Atmos., 105, 22243–22253, doi:10.1029/2000JD900299, 2000.

Bergan, T. and Rodhe, H.: Oxidation of elemental mercury in the atmosphere; constraints imposed by global scale modelling, J. Atmos. Chem., 40, 191–212, 2001.

Bergan, T., Gallardo, L., and Rodhe, H.: Mercury in the global troposphere: a three-dimensional model study, Atmos. Environ., 33, 1575–1585, 1999.

Chang, J. C. and Hanna, S. R.: Air quality model performance evaluation, Meteorol. Atmos. Phys., 87, 167–196, doi:10.1007/s00703-003-0070-7, 2004.

Clarkson, T. W.: The toxicity of mercury and its compounds, in: Mercury Pollution: Integration and Synthesis, edited by: Watras, C. J. and Huckabee, J. W., Boca Raton, FL, USA, 631–641, 1994.

Cziczo, D. J., Nowak, J. B., Hu, J. H., and Abbatt, J. P. D.: Infrared spectroscopy of model tropospheric aerosols as a function of relative humidity: observation of deliquescence and crystallization, J. Geophys. Res.-Atmos., 102, 18843–18850, 1997.

Dibble, T. S., Zelie, M. J., and Mao, H.: Thermodynamics of reactions of ClHg and BrHg radicals with atmospherically abundant free radicals, Atmos. Chem. Phys., 12, 10271–10279, doi:10.5194/acp-12-10271-2012, 2012.

Donohoue, D. L., Bauer, D., and Hynes, A. J.: Temperature and pressure dependent rate coefficients for the reaction of Hg with Cl and the reaction of Cl with Cl: a pulsed laser photolysispulsed laser induced fluorescence Study, J. Phys. Chem. A, 109, 7732–7741, 2005.

Finlayson-Pitts, B. J.: Halogens in the troposphere, Anal. Chem., 82, 770–776, doi:10.1021/ac901478p, 2010.

Finley, B. D. and Saltzman, E. S.: Observations of Cl_2, Br_2, and I_2 in coastal marine air, J. Geophys. Res., 113, D21301, doi:10.1029/2008JD010269, 2008.

Fischer, E. V., Ziemba, L. D., Talbot, R. W., Dibb, J. E., Griffin, R. J., Husain, L., and Grant, A. N.: Aerosol major ion record at Mount Washington, J. Geophys. Res.-Atmos., 112, D02303, doi:10.1029/2006JD007253, 2007.

Ghosal, S., Brown, M. A., Bluhm, H., Krisch, M. J., Salmeron, M., Jungwirth, P., and Hemminger, J. C.: Ion partitioning at the liquid/vapor interface of a multicomponent alkali halide solution: a model for aqueous sea salt aerosols, J. Phys. Chem. A, 112, 12378–12384, 2008.

Glasow, R. V., Sander, R., Bott, A., and Crutzen, P. J.: Modeling halogen chemistry in the marine boundary layer 1. Cloud-free MBL, J. Geophys. Res.-Atmos., 107, 9-1–9-16, 2002.

Goodsite, M. E., Plane, J. M. C., and Skov, H.: A theoretical study of the oxidation of HgO to $HgBr_2$ in the troposphere, Environ. Sci. Technol., 38, 1772–1776, 2004.

Goodsite, M. E., Plane, J. M. C., and Skov, H.: Erratum: A theoretical study of the oxidation of HgO to $HgBr_2$ in the troposphere, (Environ. Sci. Technol., 38, 1772–1776, doi:10.1021/es034680s, 2004), Environ. Sci. Technol., 46, 5262, doi:10.1021/es301201c, 2012.

Guha, S. and Francisco, J. S.: An ab initio study of the pathways for the reaction between CH_3O_2 and BrO radicals, J. Chem. Phys., 118, 1779–1793, doi:10.1063/1.1531099, 2003.

Gustin, M. S., Huang, J., Miller, M. B., Peterson, C., Jaffe, D. A., Ambrose, J., Finley, B. D., Lyman, S. N., Call, K., Talbot, R., Feddersen, D., Mao, H., and Lindberg, S. E.: Do we understand what the mercury speciation instruments are actually measuring? Results of RAMIX, Environ. Sci. Technol., 47, 7295–7306, 2013.

Gustin, M. S., Amos, H. M., Huang, J., Miller, M. B., and Heidecorn, K.: Measuring and modeling mercury in the atmosphere: a critical review, Atmos. Chem. Phys., 15, 5697–5713, doi:10.5194/acp-15-5697-2015, 2015.

Hall, B.: The gas phase oxidation of elemental mercury by ozone, Water Air Soil Poll., 80, 301–315, 1995.

Hanna, S. R.: Air quality model evaluation and uncertainty, JAPCA J. Air Waste Ma., 38, 406–412, doi:10.1080/08940630.1988.10466390, 1988.

Hanna, S. R., Strimaitis, D. G., and Chang, J. C.: Hazard response modeling uncertainty (a quantitative method), vol. I: User's guide for software for evaluating hazardous gas dispersion models; vol. II: Evaluation of commonly-used hazardous gas dispersion models; vol. III: Components of uncertainty in hazardous gas dispersion models, Sigma Research Corporation, Westford, USA, 1991.

Hanna, S. R., Chang, J. C., and Strimaitis, D. G.: Hazardous gas model evaluation with field observations, Atmos. Environ. A-Gen., 27, 2265–2285, doi:10.1016/0960-1686(93)90397-H, 1993.

Hedgecock, I. M. and Pirrone, N.: Chasing quicksilver: modeling the atmospheric lifetime of $Hg^0(g)$ in the marine boundary layer at various latitudes, Environ. Sci. Technol., 38, 69–76, 2004.

Hedgecock, I. M. and Pirrone, N.: Modelling Chemical and Physical Processes of Hg Compounds in the Marine Boundary Layer, in: Dynamics of Mercury Pollution on Regional and Global Scales: Atmospheric Processes and Human Exposures Around the World, edited by: Pirrone, N. and Mahaffey, K. R., Springer US, Boston, MA, USA, 295–317, doi:10.1007/0-387-24494-8_13, 2005.

Hedgecock, I. M., Pirrone, N., Sprovieri, F., and Pesenti, E.: Reactive gaseous mercury in the marine boundary layer: modelling and experimental evidence of its formation in the Mediterranean region, Atmos. Environ., 37, S41–S49, 2003.

Hess, M., Krieger, U. K., Marcolli, C., Huthwelker, T., Ammann, M., Lanford, W. A., and Peter, T.: Bromine enrichment in the near-surface region of Br-doped NaCl single crystals diagnosed by rutherford backscattering spectrometry, J. Phys. Chem. A, 111, 4312–4321, 2007.

Holmes, C. D., Jacob, D. J., and Yang, X.: Global lifetime of elemental mercury against oxidation by atomic bromine in the free troposphere, Geophys. Res. Lett., 33, L20808, doi:10.1029/2006GL027176, 2006.

Holmes, C. D., Jacob, D. J., Mason, R. P., and Jaffe, D. A.: Sources and deposition of reactive gaseous mercury in the marine atmosphere, Atmos. Environ., 43, 2278–2285, 2009.

Holmes, C. D., Jacob, D. J., Corbitt, E. S., Mao, J., Yang, X., Talbot, R., and Slemr, F.: Global atmospheric model for mercury including oxidation by bromine atoms, Atmos. Chem. Phys., 10, 12037–12057, doi:10.5194/acp-10-12037-2010, 2010.

Huang, J. and Gustin, M. S.: Uncertainties of Gaseous Oxidized Mercury Measurements Using KCl-Coated Denuders, Cation-Exchange Membranes, and Nylon Membranes: Humidity Influences, Environ. Sci. Technol., 49, 6102–6108, doi:10.1021/acs.est.5b00098, 2015.

Huang, J., Miller, M. B., Weiss-Penzias, P., and Gustin, M. S.: Comparison of gaseous oxidized Hg measured by KCl-coated denuders, and nylon and cation exchange membranes, Environ. Sci. Technol., 47, 7307–7316, 2013.

Jaffe, D. A., Lyman, S., Amos, H. M., Gustin, M. S., Huang, J., Selin, N. E., Levin, L., ter Schure, A., Mason, R. P., Talbot, R., Rutter, A., Finley, B., Jaeglé, L., Shah, V., McClure, C., Ambrose, J., Gratz, L., Lindberg, S., Weiss-Penzias, P., Sheu, G.-R., Feddersen, D., Horvat, M., Dastoor, A., Hynes, A. J., Mao, H., Sonke, J. E., Slemr, F., Fisher, J. A., Ebinghaus, R., Zhang, Y., and Edwards, G.: Progress on understanding atmospheric mercury hampered by uncertain measurements, Environ. Sci. Technol., 48, 7204–7206, doi:10.1021/es5026432, 2014.

Kim, P.-R., Han, Y.-J., Holsen, T. M., and Yi, S.-M.: Atmospheric particulate mercury: concentrations and size distributions, Atmos. Environ., 61, 94–102, 2012.

Kim, S. Y., Talbot, R., Mao, H., Blake, D. R., Huey, G., and Weinheimer, A. J.: Chemical transformations of Hg° during Arctic mercury depletion events sampled from the NASA DC-8, Atmos. Chem. Phys. Discuss., 10, 10077–10112, doi:10.5194/acpd-10-10077-2010, 2010.

Kutsher, J., Haikin, N., Sharon, A., and Heifetz, E.: On the formation of an elevated nocturnal inversion layer in the presence of a low-level jet: a case study, Bound.-Lay. Meteorol., 144, 441–449, doi:10.1007/s10546-012-9720-y, 2012.

Laskin, A., Moffet, R. C., Gilles, M. K., Fast, J. D., Zaveri, R. A., Wang, B., Nigge, P., and Shutthanandan, J.: Tropospheric chemistry of internally mixed sea salt and organic particles: surprising reactivity of NaCl with weak organic acids, J. Geophys. Res.-Atmos., 117, D15302, doi:10.1029/2012JD017743, 2012.

Laurier, F. and Mason, R.: Mercury concentration and speciation in the coastal and open ocean boundary layer, J. Geophys. Res.-Atmos., 112, D06302, doi:10.1029/2006JD007320, 2007.

Laurier, F. J. G., Mason, R. P., Whalin, L., and Kato, S.: Reactive gaseous mercury formation in the North Pacific Ocean's marine boundary layer: a potential role of halogen chemistry, J. Geophys. Res.-Atmos., 108, ACH3-1–ACH3-12, doi:10.1029/2003JD003625, 2003.

Lewis, E. R. and Schwartz, S. E.: Comment on "Size distribution of sea-salt emissions as a function of relative humidity," Atmos. Environ., 40, 588–590, doi:10.1016/j.atmosenv.2005.08.043, 2006.

Lin, C.-J. and Pehkonen, S. O.: Aqueous phase reactions of mercury with free radicals and chlorine: implications for atmospheric mercury chemistry, Chemosphere, 38, 1253–1263, 1999.

Lin, C.-J., Pongprueksa, P., Lindberg, S. E., Pehkonen, S. O., Byun, D., and Jang, C.: Scientific uncertainties in atmospheric mercury models I: Model science evaluation, Atmos. Environ., 40, 2911–2928, 2006.

Lindberg, S. E., Brooks, S., Lin, C.-J., Scott, K. J., Landis, M. S., Stevens, R. K., Goodsite, M., and Richter, A.: Dynamic oxidation of gaseous mercury in the arctic troposphere at polar sunrise, Environ. Sci. Technol., 36, 1245–1256, 2002.

Lyman, S. N., Jaffe, D. A., and Gustin, M. S.: Release of mercury halides from KCl denuders in the presence of ozone, Atmos. Chem. Phys., 10, 8197–8204, doi:10.5194/acp-10-8197-2010, 2010.

Madronich, S.: UV radiation in the natural and perturbed atmosphere, in: Environmental Effects of UV, CRC Press, Boca Raton, FL, USA, available at: http://opensky.library.ucar.edu/collections/OSGC-000-000-020-698 (last access: 16 April 2015), 1993.

Mao, H. and Talbot, R.: O_3 and CO in New England: temporal variations and relationships, J. Geophys. Res.-Atmos., 109, D21304, doi:10.1029/2004JD004913, 2004.

Mao, H. and Talbot, R.: Speciated mercury at marine, coastal, and inland sites in New England – Part 1: Temporal variability, Atmos. Chem. Phys., 12, 5099–5112, doi:10.5194/acp-12-5099-2012, 2012.

Mao, H., Talbot, R. W., Sigler, J. M., Sive, B. C., and Hegarty, J. D.: Seasonal and diurnal variations of Hg° over New England, Atmos. Chem. Phys., 8, 1403–1421, doi:10.5194/acp-8-1403-2008, 2008.

Mao, H., Talbot, R., Hegarty, J., and Koermer, J.: Speciated mercury at marine, coastal, and inland sites in New England – Part 2: Relationships with atmospheric physical parameters, Atmos. Chem. Phys., 12, 4181–4206, doi:10.5194/acp-12-4181-2012, 2012.

Mason, R. P., Kim, E.-H., Cornwell, J., and Heyes, D.: An examination of the factors influencing the flux of mercury, methylmercury and other constituents from estuarine sediment, Mar. Chem., 102, 96–110, 2006.

McClure, C. D., Jaffe, D. A., and Edgerton, E. S.: Evaluation of the KCl Denuder Method for Gaseous Oxidized Mercury using $HgBr_2$ at an In-Service AMNet Site, Environ. Sci. Technol., 48, 11437–11444, doi:10.1021/es502545k, 2014.

Miller, C. L., Mason, R. P., Gilmour, C. C., and Heyes, A.: Influence of dissolved organic matter on the complexation of mercury under sulfidic conditions, Environ. Toxicol. Chem., 26, 624–633, 2007.

Moldanová, J. and Ljungström, E.: Sea-salt aerosol chemistry in coastal areas: a model study, J. Geophys. Res.-Atmos., 106, 1271–1296, doi:10.1029/2000JD900462, 2001.

Obrist, D., Tas, E., Peleg, M., Matveev, V., Faïn, X., Asaf, D., and Luria, M.: Bromine-induced oxidation of mercury in the mid-latitude atmosphere, Nat. Geosci., 4, 22–26, 2011.

Pal, B. and Ariya, P. A.: Gas-phase HO-initiated reactions of elemental mercury: kinetics, product studies, and atmospheric implications, Environ. Sci. Technol., 38, 5555–5566, 2004a.

Pal, B. and Ariya, P. A.: Studies of ozone initiated reactions of gaseous mercury: kinetics, product studies, and atmospheric implications, Phys. Chem. Chem. Phys., 6, 572–579, 2004b.

Pillai, P. S. and Moorthy, K. K.: Aerosol mass-size distributions at a tropical coastal environment: response to mesoscale and synoptic processes, Atmos. Environ., 35, 4099–4112, doi:10.1016/S1352-2310(01)00211-4, 2001.

Poissant, L., Pilote, M., Beauvais, C., Constant, P., and Zhang, H. H.: A year of continuous measurements of three atmospheric mercury species (GEM, RGM and Hgp) in southern Québec, Canada, Atmos. Environ., 39, 1275–1287, 2005.

Raofie, F. and Ariya, P. A.: Product study of the gas-phase BrO-initiated oxidation of Hg^0: Evidence for stable Hg^{1+} compounds, Environ. Sci. Technol., 38, 4319–4326, 2004.

Rolfhus, K. R., Sakamoto, H. E., Cleckner, L. B., Stoor, R. W., Babiarz, C. L., Back, R. C., Manolopoulos, H., and Hurley, J. P.: Distribution and fluxes of total and methylmercury in Lake Superior, Environ. Sci. Technol., 37, 865–872, 2003.

Rutter, A. P. and Schauer, J. J.: The impact of aerosol composition on the particle to gas partitioning of reactive mercury, Environ. Sci. Technol., 41, 3934–3939, doi:10.1021/es062439i, 2007.

Rutter, A. P., Shakya, K. M., Lehr, R., Schauer, J. J., and Griffin, R. J.: Oxidation of gaseous elemental mercury in the presence of secondary organic aerosols, Atmos. Environ., 59, 86–92, 2012.

Saiz-Lopez, A. and von Glasow, R.: Reactive halogen chemistry in the troposphere, Chem. Soc. Rev., 41, 6448–6472, doi:10.1039/C2CS35208G, 2012.

Saiz-Lopez, A., Shillito, J. A., Coe, H., and Plane, J. M. C.: Measurements and modelling of I_2, IO, OIO, BrO and NO_3 in the mid-latitude marine boundary layer, Atmos. Chem. Phys., 6, 1513–1528, doi:10.5194/acp-6-1513-2006, 2006.

Sander, R., Keene, W. C., Pszenny, A. A. P., Arimoto, R., Ayers, G. P., Baboukas, E., Cainey, J. M., Crutzen, P. J., Duce, R. A., Hönninger, G., Huebert, B. J., Maenhaut, W., Mihalopoulos, N., Turekian, V. C., and Van Dingenen, R.: Inorganic bromine in the marine boundary layer: a critical review, Atmos. Chem. Phys., 3, 1301–1336, doi:10.5194/acp-3-1301-2003, 2003.

Sander, S. P., Abbatt, J., Barker, J. R., Burkholder, J. B., Friedl, R. R., Golden, D. M., Huie, R. E., Kolb, C. E., Kurylo, M. J., Moortgat, G. K., Orkin, V. L., and Wine, P. H.: Chemical Kinetics and Photochemical Data for Use in Atmospheric Studies, Evaluation No. 17, JPL Publication 10-6, Jet Propulsion Laboratory, Pasadena, USA, available at: http://jpldataeval.jpl.nasa.gov (last access: 1 July 2016), 2011.

Sandu, A. and Sander, R.: Technical note: Simulating chemical systems in Fortran90 and Matlab with the Kinetic PreProcessor KPP-2.1, Atmos. Chem. Phys., 6, 187–195, doi:10.5194/acp-6-187-2006, 2006.

Schroeder, W. H. and Munthe, J.: Atmospheric mercury – an overview, Atmos. Environ., 32, 809–822, 1998.

Schwartz, S. E.: Mass-transport considerations pertinent to aqueous phase reactions of gases in liquid-water clouds, in: Chemistry of Multiphase Atmospheric Systems, edited by: Jaeschke, D. W., Springer, Berlin, Heidelberg, Germany, 415–471, available at: http://link.springer.com/chapter/10.1007/978-3-642-70627-1_16 (last access: 17 April 2015), 1986.

Selin, N. E., Javob, D. J., Park, R. J., Yantosca, R. M., Strode, S., Jaeglé, L., and Jaffe, D.: Chemical cycling and deposition of atmospheric mercury: global constraints from observations, J. Geophys. Res.-Atmos., 112, D02308, doi:10.1029/2006JD007450, 2007.

Seigneur, C., Wrobel, J., and Constantinou, E.: A chemical kinetic mechanism for atmospheric inorganic mercury, Environ. Sci. Technol., 28, 1589–1597, 1994.

Shon, Z.-H., Kim, K.-H., Kim, M.-Y., and Lee, M.: Modeling study of reactive gaseous mercury in the urban air, Atmos. Environ., 39, 749–761, 2005.

Sigler, J. M., Mao, H., and Talbot, R.: Gaseous elemental and reactive mercury in Southern New Hampshire, Atmos. Chem. Phys., 9, 1929–1942, doi:10.5194/acp-9-1929-2009, 2009.

Sillman, S., Marsik, F. J., Al-Wali, K. I., Keeler, G. J., and Landis, M. S.: Reactive mercury in the troposphere: model formation and results for Florida, the northeastern United States, and the Atlantic Ocean, J. Geophys. Res.-Atmos., 112, D23305, doi:10.1029/2006JD008227, 2007.

Simpson, W. R., von Glasow, R., Riedel, K., Anderson, P., Ariya, P., Bottenheim, J., Burrows, J., Carpenter, L. J., Frieß, U., Goodsite, M. E., Heard, D., Hutterli, M., Jacobi, H.-W., Kaleschke, L., Neff, B., Plane, J., Platt, U., Richter, A., Roscoe, H., Sander, R., Shepson, P., Sodeau, J., Steffen, A., Wagner, T., and Wolff, E.: Halogens and their role in polar boundary-layer ozone depletion, Atmos. Chem. Phys., 7, 4375–4418, doi:10.5194/acp-7-4375-2007, 2007.

Simpson, W. R., Brown, S. S., Saiz-Lopez, A., Thornton, J. A., and von Glasow, R.: Tropospheric halogen chemistry: sources, cycling, and impacts, Chem. Rev., 115, 4035–4062, doi:10.1021/cr5006638, 2015.

Snider, G., Raofie, F., and Ariya, P. A.: Effects of relative humidity and CO(g) on the O_3-initiated oxidation reaction of HgO(g): kinetic and product studies, Phys. Chem. Chem. Phys., 10, 5616–5623, 2008.

Soerensen, A. L., Sunderland, E. M., Holmes, C. D., Jacob, D. J., Yantosca, R. M., Skov, H., Christensen, J. H., Strode, S. A., and Mason, R. P.: An improved global model for air–sea exchange of mercury: high concentrations over the North Atlantic, Environ. Sci. Technol., 44, 8574–8580, 2010.

Steffen, A., Douglas, T., Amyot, M., Ariya, P., Aspmo, K., Berg, T., Bottenheim, J., Brooks, S., Cobbett, F., Dastoor, A., Dommergue, A., Ebinghaus, R., Ferrari, C., Gardfeldt, K., Goodsite, M. E., Lean, D., Poulain, A. J., Scherz, C., Skov, H., Sommar, J., and Temme, C.: A synthesis of atmospheric mercury depletion event chemistry in the atmosphere and snow, Atmos. Chem. Phys., 8, 1445–1482, doi:10.5194/acp-8-1445-2008, 2008.

Subir, M., Ariya, P. A., and Dastoor, A. P.: A review of uncertainties in atmospheric modeling of mercury chemistry I. Uncertainties in existing kinetic parameters – fundamental limitations and the importance of heterogeneous chemistry, Atmos. Environ., 45, 5664–5676, 2011.

Talbot, R., Mao, H., and Sive, B.: Diumal characteristics of surface level O_3 and other important trace gases in New England, J. Geophys. Res., 110, D09307, doi:10.1029/2004JD005449, 2005.

Tang, I. N., Tridico, A. C., and Fung, K. H.: Thermodynamic and optical properties of sea salt aerosols, J. Geophys. Res.-Atmos., 102, 23269–23275, 1997.

Tokos, J. J. S., Hall, B., Calhoun, J. A., and Prestbo, E. M.: Homogeneous gas-phase reaction of HgO with H_2O_2, O_3, CH_3I, and $(CH_3)_2S$: implications for atmospheric Hg cycling, Atmos. Environ., 32, 823–827, 1998.

Toyota, K., McConnell, J. C., Staebler, R. M., and Dastoor, A. P.: Air–snowpack exchange of bromine, ozone and mercury in

the springtime Arctic simulated by the 1-D model PHANTAS – Part 1: In-snow bromine activation and its impact on ozone, Atmos. Chem. Phys., 14, 4101–4133, doi:10.5194/acp-14-4101-2014, 2014.

University of New Hampshire: AIRMAP Observing Network program, available at: http://www.eos.unh.edu/observatories/data.shtml, last access: 8 July 2016.

Verwer, J. G., Spee, E. J., Blom, J. G., and Hundsdorfer, W.: Second-order Rosenbrock method applied to photochemical dispersion problems, SIAM J. Sci. Comput., 20, 1456–1480, 1999.

Wang, F., Saiz-Lopez, A., Mahajan, A. S., Gómez Martín, J. C., Armstrong, D., Lemes, M., Hay, T., and Prados-Roman, C.: Enhanced production of oxidised mercury over the tropical Pacific Ocean: a key missing oxidation pathway, Atmos. Chem. Phys., 14, 1323–1335, doi:10.5194/acp-14-1323-2014, 2014.

Weiss-Penzias, P., Jaffe, D. A., McClintick, A., Prestbo, E. M., and Landis, M. S.: Gaseous elemental mercury in the marine boundary layer: evidence for rapid removal in anthropogenic pollution, Environ. Sci. Technol., 37, 3755–3763, 2003.

Xie, Z.-Q., Sander, R., Pöschl, U., and Slemr, F.: Simulation of atmospheric mercury depletion events (AMDEs) during polar springtime using the MECCA box model, Atmos. Chem. Phys., 8, 7165–7180, doi:10.5194/acp-8-7165-2008, 2008.

Zhang, L., Wright, L. P., and Blanchard, P.: A review of current knowledge concerning dry deposition of atmospheric mercury, Atmos. Environ., 43, 5853–5864, 2009.

Zhang, L., Blanchard, P., Gay, D. A., Prestbo, E. M., Risch, M. R., Johnson, D., Narayan, J., Zsolway, R., Holsen, T. M., Miller, E. K., Castro, M. S., Graydon, J. A., Louis, V. L. St., and Dalziel, J.: Estimation of speciated and total mercury dry deposition at monitoring locations in eastern and central North America, Atmos. Chem. Phys., 12, 4327–4340, doi:10.5194/acp-12-4327-2012, 2012.